Component Based Normalization for PET Systems with Depth of Interaction Measurement Capability

Angela M K Foudray, *Student Member, IEEE,* Garry Chinn, *Member, IEEE* and Craig S Levin, *Member, IEEE*

***Abstract*— The number of lines of response (LOR) in a system with small crystals and depth of interaction (DOI) measurement capability can require prohibitive amounts of memory and computational resources. The number of independent LORs in the small animal imaging system evaluated in this study is ~2 x 10^9. We propose a method to adapt the component-based normalization model to include (1) DOI and (2) large field of view (FOV) to system inner bore volume percentage (near 100%) or percentage of view (POV) considerations without an order of magnitude increase in computational resources. This method can also compensate for bin location errors made during the LOR calculation. Included in the study were radial, axial and interference geometric efficiency and crystal absorption factors. We have observed a large effect on sensitivity from axial geometric factors, distance between positioned coincident photon interactions, and amount of crystal surrounding any particular crystal in our system. Assessing direct plane sinograms of direct normalization data (infinitely thin cylindrical annulus), we have observed that there are LORs that received zero counts due to inter-module gaps. Component based normalization pre-correction weights significantly improved the coefficient of variation for the reconstructed 1.5 mm and 1.75 mm spheres in the row nearest the center line in the axial image slices by 17%, 32%, and 51% in the z = 0 cm, z = 1.5 cm, and z = 3.0 cm axial planes, respectively.**

***Index Terms*— Normalization, Component-Based, Depth of Interaction, Positron Emission Tomography, Small Animal, Dedicated Breast, Monte Carlo, GATE**

I. Introduction

In order to achieve good image quality and quantitative accuracy in positron emission tomography (PET) reconstructed images, the sensitivity of each detector line of response (LOR) must be normalized. There are two commonly used methods for calculating a weighting factor to apply to binned data before reconstruction: direct normalization and component-based normalization. Direct normalization is time consuming and does not account for the difference between the normalization factors for scatter and true coincidence events [1]. Also, direct normalization assumptions break down when the useful field of view (FOV) becomes a significant portion of the viewable area of the system. We are using detectors that have 3D positioning capability. We propose to move the detectors in close to the imaging subject for higher sensitivity, leading to a usable FOV equal to the interior dimensions of the system. Component based normalization was introduced to take all the factors into account that contribute to the efficiency of a particular LOR [2]. Here we propose a method to adapt the component-based normalization model to include depth of interaction (DOI) and large useful FOV considerations without an order of magnitude increase in computational resources.

Manuscript received November 11, 2005. This work was supported in part by NIH-NCI grant R21 CA098691 and NIH-NIBIB grant R21 EB003283.

Angela MK Foudray is with the Department of Radiology, the Molecular Imaging Program at Stanford University and the Department of Physics at the University of California, San Diego (afoudray@stanford.edu). Garry Chinn and Craig S Levin are in the Department of Radiology, the Molecular Imaging Program at Stanford University.

II. Theory

Component-based normalization models compute the activity within a LOR using the following relationship [2]:

$$A_i \quad C(P,R,S)NC(true)_i att_i dt_i \tag{1}$$

where A is the activity; i is the index of the LOR; P is prompt, R is random, S is the scatter count rate; C is a rate dependent on the count rates P, R and S; NC(true) is the normalization coefficient for true coincidences; and att and dt are the attenuation and dead-time correction factors. The normalization coefficient can be broken down further into components based on variations of intrinsic efficiencies (ϵ) such as crystal and photodetector imperfections, which vary for each crystal, and geometric efficiencies (g) such as solid angle variation versus annihilation location along the LOR. Please note: in this paper, as per convention in component-based normalization literature [2], the crystal absoprtion probabilty ($e^{-\mu x}$) as a function of angle is included in the g rather than ϵ factors. These factors can also be represented as multiplicative coefficients to compute the NC:

$$NC_i = \epsilon_i g_i \tag{2}$$

With depth of interaction measurement capability, the number of lines of response can require overwhelming amounts memory and computational resources. For instance, the number of independent LORs in the small animal imaging system investigated here is about $3\ (6\ 70\ 62)^2$, or about 2 billion. To reduce the matrix sizes involved in normalization and reconstruction, LORs involving deep crystal can be re-binned to detectors nearest to the FOV. Figure 1 shows this concept: the red line is the LOR from the actual interaction

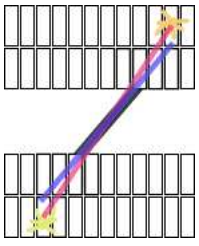

Fig. 1. Illustration of depth of interaction re-binning. Red line: actual LOR reported by the detectors, purple line: binned LOR to crystal, black line: re-binned DOI LOR

position, the purple line is the binned LOR, and the black line is the LOR resulting from re-binning to the front crystals. Re-binning the data adds or subtracts counts, or efficiency to the LOR to which the data has been binned. The NC can then be written as:

$$NC_i = \epsilon_i g_i + \sum_j \epsilon_j g_j \alpha_{ij} \quad (3)$$

where α = 1, 0 or -1. The α coefficient is 1 if LOR j is re-binned to LOR i and 0 if there is no correlation between LOR j and i. This method can also compensate for binning errors made during the LOR calculation for the acquired data by increasing (α = 1) and decreasing (α = -1) the normalization coefficient, i.e. LORs binned to LOR i during independent binning processes.

III. Methods

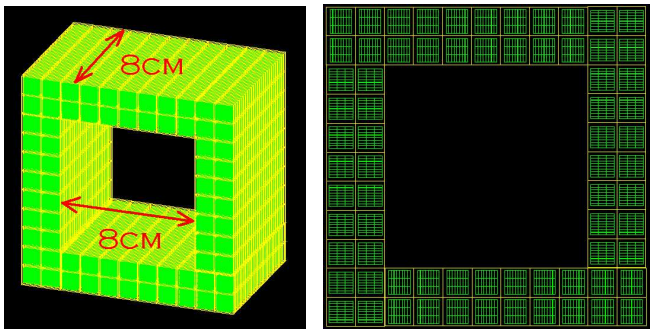

(a) Screenshot of the system during GATE simulation showing the 8cm x 8cm x 8cm field of view.

(b) Axial cross-section of the system showing the crystal placement and distance between crystal arrays. The crystals are outlined in green, the PSAPDs are outlined in yellow.

Fig. 2. System geometry illustrations

The Monte Carlo package GATE (GEANT4) was used to generate the data reported in this study. The imaging system simulated is a box-shaped small animal PET system constructed of thin (300 μm) position-sensitive avalanche photodiodes (PSAPDs) coupled to 1mm x 1mm x 3mm Lutetium Oxyorthosilicate (LSO) scintillation crystals forming an 8x3 array (dimensions 8mm x 9mm), giving the system 1mm trans-axial, 1.3 mm axial and 3mm depth of interaction positioning capability (see figure 2). The variation of intrinsic efficiency due to factors such as photodetector gain and crystal light output in the detector pairs were not modeled in the Monte Carlo, so the normalization coefficient reduces to the following geometric factors (θ: angle in XY plane, ϕ: angle from Z-axis, int: row and column crystal location based interference, c:, α, β: detectors in LOR i, dd: $\alpha\beta$ distance, w(dd): $\alpha\beta$ distance weight):

$$g_i = (g_\theta)_\alpha (g_\phi)_\alpha (g_{int})_\alpha (g_\theta)_\beta (g_\phi)_\beta (g_{int})_\beta w(dd_{\alpha\beta}) \quad (4)$$

The system comprises modules stacked together in the trans-axial and axial direction to form the system. A module is

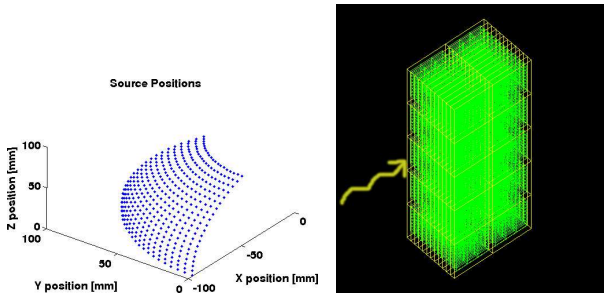

(a) (b)

Fig. 3. (a) Locations of a sphere source irradiating the section covering the axial and translational range of angles of lines of response in the detector system. (b) Section of the system modeled. Green lines: outline of the LSO crystals, yellow lines: outline of the PSAPDs, and yellow photon for reference of direction of incident photons.

made up of two PSAPDs adjacent to each other in the depth of interaction direction, each with an 8x3 array of 1mm x 1mm x 3mm LSO crystals for a total of 48 crystals in one module. One section of the box was modeled (figure 3a) and due to system symmetry, only the module in the center of the section was investigated to determine efficiencies. Events were generated for a constant time for each crystal in the module investigated, irradiated at a distance of 10cm from the center of the crystal for all θ and ϕ angles in the solid angle of the system geometry (figure 3b).

Because of the high fraction of events involving inter-crystal scatter and its affect on positioning [3], [4] and sensitivity [5], [6] of this system, multiple modules in each direction surrounding the crystal in the module being evaluated were modeled, giving a system section size of 2.2cm in the depth of interaction direction, 5.5cm in the transaxial direction and 1.6cm in the axial direction (figure 3b).

Each of the g and w terms were calculated and normalized individually so that each component weight as well as the total weight, g, had a range from 1 to infinity. Fits were made for the theta, phi and crystal position dependence on the sensitivity for each crystal in the module and their corresponding weights were generated to produce pre-corrected data for the list-mode reconstruction algorithm. We also investigated the types and number of interactions occurring in each crystal.

To evaluate the normalization algorithm, a three dimensional resolution phantom was used, consisting of three axial planes of sources. Each plane consists of spheres separated by twice their diameter. The diameter of the spheres for each quadrant are 1, 1.25, 1.5, 1.75 mm. The total activity in the phantom was 10 μCi, distributed between the three planes, with constant concentration for all spheres. The list-mode OS-EM algorithm was used with 1 iteration and 16 subsets. A 1 mm bin size was chosen, giving a Nyquist sampling rate of 2mm.

IV. Results and Discussion

A. Direct Normalization

Looking at the sinogram constructed from a cylindrical annulus of activity (figure 4a), large gaps are apparent in the

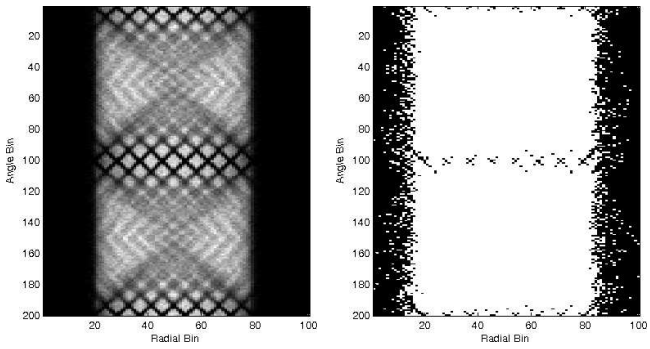

(a) Direct plane sinogram of a infinitely thin cylindrical annulus 2.5cm in radius

(b) Direct plane sinogram bins with number of counts > 0 (white)

Fig. 4. Direct plane sinograms

direct plane sinogram and there are some bins where there were no counts at all (figure 4b). These gaps are due to the absence of crystals in the dead regions surrounding each PSAPD photo-detector used in this study. The normalization factor necessary to correct for the bins with zero counts would be infinite. We are currently studying a sheet crystal design that would eliminate these dead gaps.

B. Component-Based Normalization

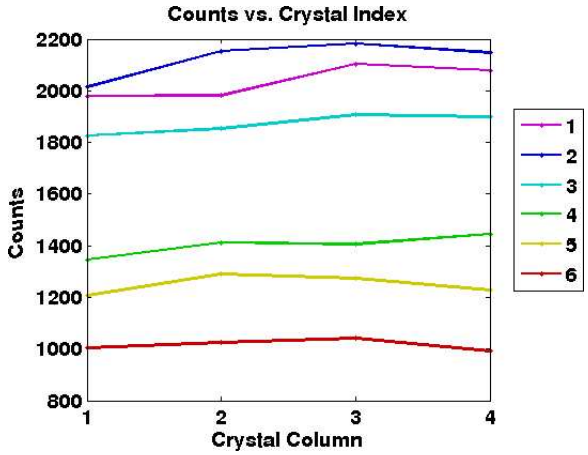

Fig. 5. Sensitivity of each of the six crystal rows in one module for a source irradiating each crystal edge-on from a distance of 10cm.

Due to symmetry of the system and the module, only half of the crystals in each row need to be studied. Crystals 1-4 are in row 1, the row nearest to the center of the system, and are in columns 1-4 respectively. Crystals 5-8 are in row 2, the next row in the depth of interaction direction, in columns 1-4, respectively, etc. Crystal 1 is at the corner of the crystal array.

The expected exponential attentuation was observed for deeper rows (figure 5), though scattering effects dominated near the front face of the module. Since events with one or more scatter interactions comprise the bulk of the events, and the scatter length is large compared to the size of one crystal, crystals surrounded by other crystal on all sides gave a higher sensitivity than crystals near any edge of the module.

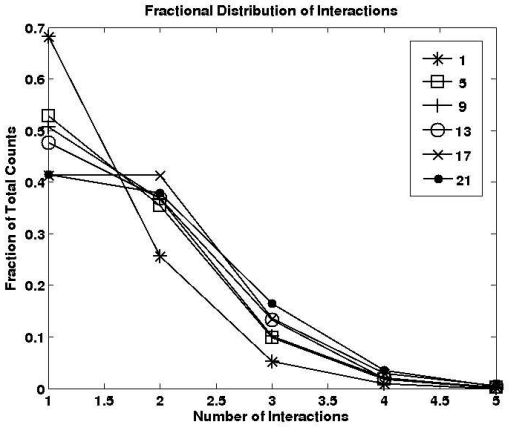

Fig. 6. Fraction of the events having the indicated number of interactions for crystals 1,5,9,13,17 and 21 in the module.

Events acquired for $\theta = \pi$ and $\phi = \pi/2$ in each of the investigated crystals and were assessed for the number of interactions the center of mass (COM) positioned photon experienced. Plotted in figure 6 is the distribution of number of interactions for the crystal in column 1 for each row in the module. As expected, the relative fraction of events containing only photoelectric interactions was the highest for row 1 (crystal 1), as there was adjacent crystal on only two sides. Deep within the module, the distribution of number of interactions is much more similar amoungst the rows.

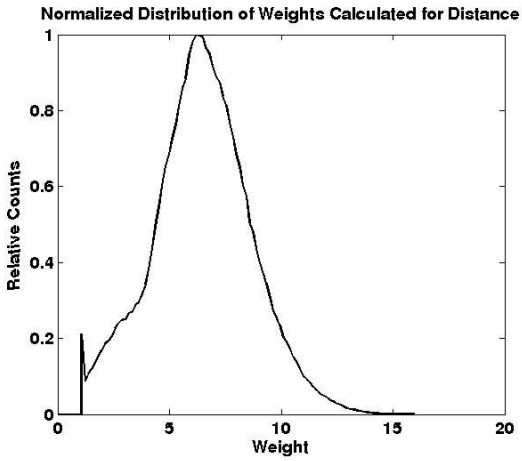

Fig. 7. Distribution of $\alpha\beta$ distance weight for the phantom with sphere sources on three axial planes.

For w($dd_\alpha\beta$), sensitivity was fit to a power function of $dd_{\alpha\beta}$ and normalized. Figure 7 shows the distribution and range of the weights for the reconstructed events for the three-plane, sphere-source phantom. This factor contributed most to the weight applied to each normalized reconstructed LOR.

Reconstructed images of a resolution phantom repeated in three axial planes are shown in figure 8. The normalized reconstructed images contain 16 million counts, which corresponds to about 0.008 counts per independent LOR, or about 0.4

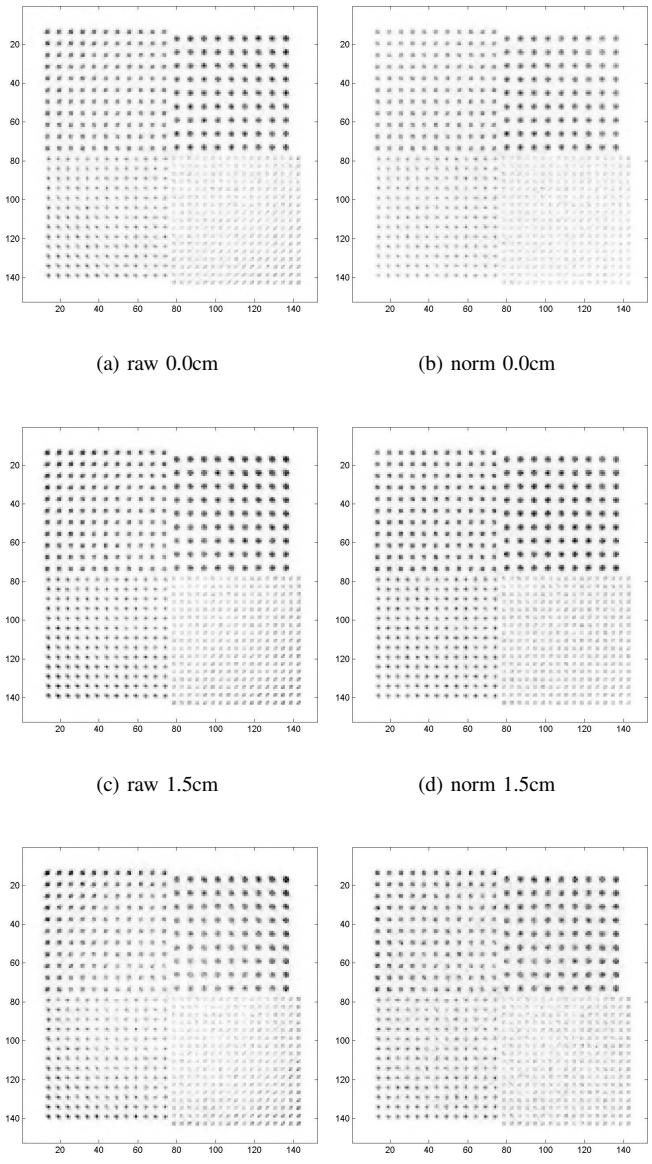

(a) raw 0.0cm (b) norm 0.0cm

(c) raw 1.5cm (d) norm 1.5cm

(e) raw 3.0cm (f) norm 3.0cm

Fig. 8. Raw (left) and normalized (right) reconstructed images for a plane of spheres at three axial locations in the FOV where norm: CB normalized, raw: un-normalized, and the distance is the axial location from the center of the system.

counts per LOR re-binned to bins closest to the FOV. Data was acquired for the three dimensional resolution phantom with spheres for all three planes concurrently and then reconstructed images were sliced axially in 1mm slices to produce the three images on the left and right of figure 8.

In the raw reconstructed images, because detectors were physically much closer in the corners of the system, reconstructed spheres in the corner of the FOV were hotter, which also contributed to hotter inter-sphere background or the impression of streaking. The inter-crystal gaps in the system contributed to the depression of the uncorrected spheres in the center of the system. After application of the normalization weights to the events, a more uniform and streak-free image was produced. This pre-correction weight significantly improved the coefficient of variation for the reconstructed 1.5 mm and 1.75 mm spheres in the row nearest the center line by 17%, 32%, and 51% in the z = 0 cm, z = 1.5 cm, and z = 3.0 cm axial planes, respectively.

V. Conclusion

We have observed a large effect on sensitivity from axial geometric factors, distance between positioned coincidence photon interactions, and amount of crystal surrounding a particular crystal in our system. This resulted in the raw reconstructed images having regions of higher than average reconstructed counts in the corner and lower than average reconstructed counts in the center of the system, as well as small streaks in regions of high sensitivity due to the repetitive structure of the phantom and the EM reconstruction algorithm used.

A component-based normalization weight was calculated for one module in one section of the system and was used to generate the weights for all LORs, which corrected the data before applying the list-mode reconstruction algorithm. This pre-correction weight significantly improved the coefficient of variation for the reconstructed spheres by 30% for the three planes investigated. In both the raw and normalized images, we were able to resolve the 1mm diameter spheres throughout the relatively large useful field of view (the spheres span the FOV to within 3mm from the edge of the detector system).

Separating the factors of the normalization coefficients can be used to accurately weight each line of response in order to obtain quantitative reconstructed images and to help illuminate the design factors affecting the design of a detector system.

Further work will include contrast recovery and three-dimensional sensitivity and resolution studies to fully compare the box-like and cylindrical geometries we are considering for the design of our small animal system.

Acknowledgment

This work was supported in part by NIH-National Cancer Institute (R21 CA098691) and NIH-NIBIB (R21 EB003283).

References

[1] J. M. Ollinger, "Detector efficiency and compton scatter in fully 3d pet," *IEEE Trans Nucl Sci*, vol. 42, no. 4, 1995.

[2] R. D. Badawi and P. K. Marsden, "Developments in component-based normalization for 3d pet," *Phys Med Bio*, vol. 44, pp. 571–594, 1999.

[3] A. M. K. Foudray, G. Chinn, C. S. Levin, and P. D. Olcott, "Investigating positioning and scatter rejection algorithms in a high resolution pet system capable of depth of interaction measurement," *Presented at the 2005 Soc Nucl Med annual meeting*, 2004.

[4] A. M. K. Foudray, G. Chinn, C. S. Levin, and P. Olcott, "Event rejection techniques for list mode positron emission tomography," *in preparation*, 2006.

[5] A. M. K. Foudray, F. Habte, G. Chinn, J. Zhang, C. S. Levin, and P. D. Olcott, "Optimization of a pet breast imaging system comprised of position sensitive avalanche photodiodes utilizing monte carlo simulation," *Presented at the 2004 IEEE NSS-MIC Breast Cancer Workshop*, 2004.

[6] A. M. K. Foudray, F. Habte, G. Chinn, J. Zhang, and C. S. Levin, "Optimization of a pet imaging system with direct depth of interaction measurement comprised of position sensitive avalanche photodiodes utilizing monte carlo simulation," *in preparation*, 2006.